Ligand-engineered Cu-based halide perovskite for highly efficient near-infrared photocatalytic CO_2 reduction

Hongmei Ran [a], Daofu Wu [b,*], Wei Chen [a], Yichen Liu [a], Liqin Gao [a], Jinchen Zhou [a], Bo Gao [f], Junan Lai [e], Heng Luo [d], Faguang Kuang [d], Min Mo [d], Zhiqiong Luo [d], Fan Dong [g], Hao Ma [h], Qian Zhang [a], Faling Ling [c,*], Baofei Sun [d,*], Xiaosheng Tang [a,e,f,**]

[a] College of Optoelectronic Engineering, Chongqing University of Posts and Telecommunications, Chongqing 400065, China
[b] State Key Laboratory of Catalysis, Dalian Institute of Chemical Physics, Chinese Academy of Sciences, Dalian 116023, China
[c] School of Science, Chongqing University of Posts and Telecommunications, Chongqing 400065, China
[d] Key Laboratory of Human Brain bank for Functions and Diseases of Department of Education of Guizhou Province, College of Basic Medical, Guizhou Medical University, Guiyang 550025, China
[e] Key Laboratory of Optoelectronic Technology & Systems (Ministry of Education), College of Optoelectronic Engineering, Chongqing University, Chongqing 400044, China
[f] School of Materials Science and Engineering, Zhengzhou University, Zhengzhou 450001, China
[g] Institute of Fundamental and Frontier Sciences, University of Electronic Science and Technology of China, Chengdu 611731, China
[h] National Research Base of Intelligent Manufacturing Service, Chongqing Technology and Business University, Chongqing 400067, China

ARTICLE INFO

ABSTRACT

A key challenge in harvesting solar energy for efficient chemical conversion is the lack of photocatalysts with wide activation wavelengths. Herein, we propose for the first time to utilize halide perovskite to absorb the full spectrum (200–2500 nm), including ultraviolet (UV), visible (Vis), and near-infrared (NIR) light, to directly power photocatalytic CO_2 reduction. This full-spectrum light-responsive occurs on metal halide perovskite Cs_2CuCl_4 microcrystals (MCs), and the ligand soybean lecithin is applied to optimize the active phase of Cs_2CuCl_4 photocatalyst, such as morphology, particle size, crystal face and electronic structure. As revealed by optical absorption analysis, the Cs_2CuCl_4 and ligand soybean lecithin modified Cs_2CuCl_4 (SL-Cs_2CuCl_4) MCs exhibit significant optical absorption in the UV, Vis light and NIR light regions. The photocatalytic CO_2 reduction performance was assessed under simulated sunlight (200–2500 nm), and the SL-Cs_2CuCl_4 MCs achieved a CO fuel yield of 254.46 µmol g^{-1}, which increased the yield by 5 times relative to the initial sample. Based on in-situ Fourier transform infrared, electron spin resonance and X-ray photoelectron spectroscopy, the active substances and reaction intermediates at the active site of SL-Cs_2CuCl_4 MCs were dynamically monitored, and the photocatalytic mechanism was revealed together with density functional theory (DFT) calculations. The DFT calculation shows that the photocatalytic reduction of CO_2 to CO by Cs_2CuCl_4 is proposed to involve the concerted action of both Cs and Cu sites.

1. Introduction

With increasing energy shortages and environmental concerns, harnessing inexhaustible solar energy is seen as an attractive strategy to drive the conversion of CO_2 into value-added chemical fuel [1–4]. Photocatalysis, a promising technology that uses ubiquitous intermittent sunlight to convert atmospheric CO_2 into a sustainable fuel, has received widespread concern [5–8]. However, the most advanced photocatalytic systems are still in their infancy and far from the requirements of industrialization, the underutilization of solar energy is one of the important reasons. Most commonly used photocatalysts can only utilize the ultraviolet-visible (UV-Vis) band of the solar spectrum, while ultraviolet and visible light account for only 4% and 46% of solar radiation, respectively, and the infrared band, which accounts for about 50% of the solar spectrum, has long been underutilized [9–11].

In recent years, researchers have proposed some strategies to

---

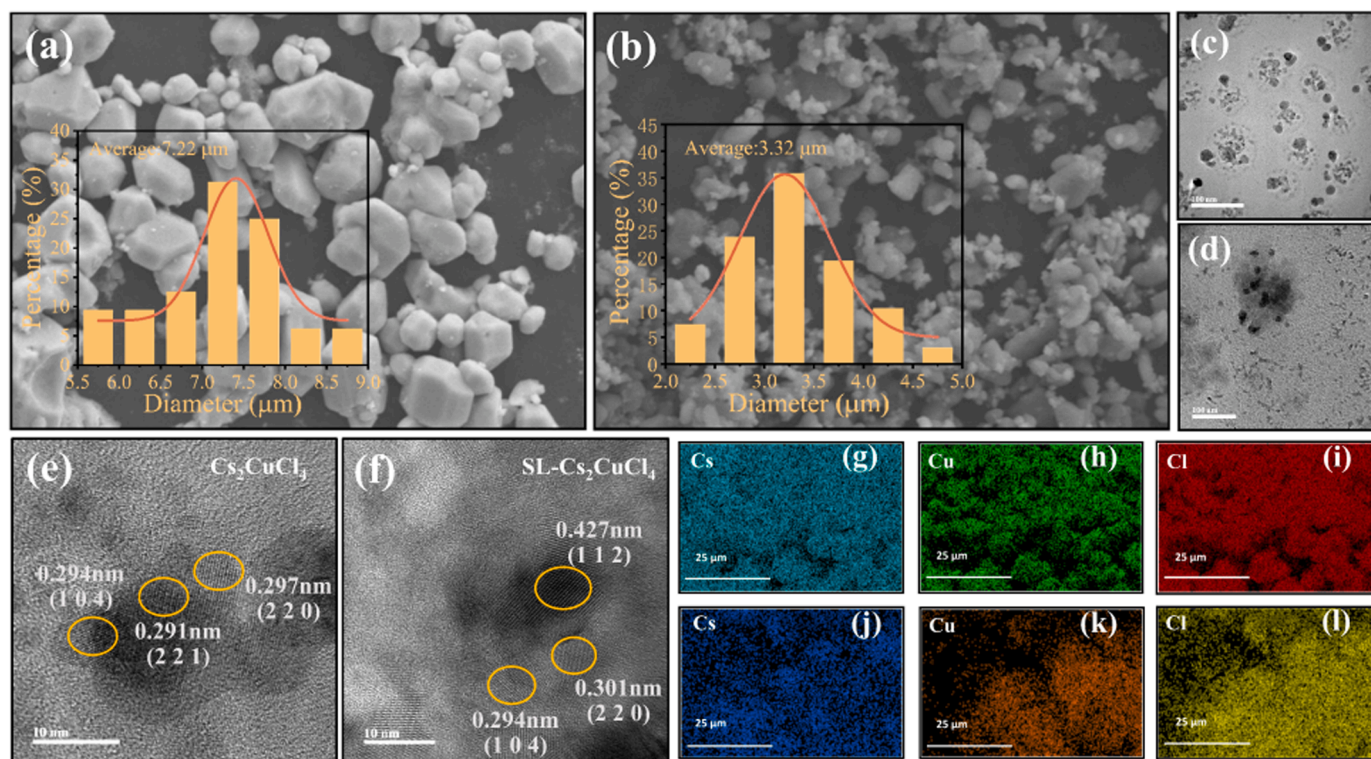**Fig. 1.** (a, b) SEM images of Cs_2CuCl_4 and SL-Cs_2CuCl_4 MCs. (c, d) TEM images of Cs_2CuCl_4 and SL-Cs_2CuCl_4 MCs. (e, f) HRTEM images of Cs_2CuCl_4 and SL-Cs_2CuCl_4 MCs. (g-i) EDS mapping images of the Cs_2CuCl_4 MCs. (j-l) EDS mapping images of the SL-Cs_2CuCl_4 MCs.

construct photocatalytic systems that can capture near-infrared photons [12,13]. But so far, few articles have reported photocatalyst that can directly absorb the near-infrared band. Halide perovskites are considered as ideal high-performance photocatalysts due to their suitable band gap, high light absorption efficiency and excellent charge transport characteristics across a wide spectrum, and their easy-to-customize composition, structure and morphology [14–19]. Although significant advances in the field of photocatalysis have been reported with perovskites [14,19–23], the development of stable, full-band light-driven CO_2 emission reduction photocatalysts with high light conversion efficiency remains critical.

Ligand modification can improve the stability of materials, regulate the shape/size of particles, and control the growth of crystal faces [24–28], and has been widely used in photocatalysis. For instance, Ahlawat et al.[18] designed a multifunctional affinity ligand (NKE-12) with multi-dentate ionic groups at both ends, which significantly improves the colloidal stability of $CsPbBr_3$ in aqueous media without compromising its structural integrity and catalytic properties. Hua et al. [28] demonstrated that the surface blocking effect of end-sealing ligand on the reduction behavior of Cu_2O nanoparticles is influenced by the type of end-sealing ligand. The stability of the photocatalyst and the direct use of infrared light to enhance the photocatalytic CO_2 reduction reaction need to be further explored. Therefore, it is particularly important to find materials with favorable stability and near-infrared light absorption to achieve ideal CO_2 emission reduction. Transition metal copper has the characteristics of environmentally friendly, low cost [29]. Even more encouraging, Cu exhibits excellent multi-electron reduction capabilities in CO_2 photoreduction, such as reducing CO_2 to CH_4[30]. For Cu^{2+}, Shen et al.[31] constructed a photocatalyst based on Cu-based halide perovskite Cs_2CuBr_4, revealing that the synergistic enhancement of microelectronic polarization in Cs_2CuBr_4 induced by surface-suppressed Lewis pair-like properties and intrinsic Cu d-band properties promotes strong CO_2 adsorption and activation. But to our knowledge, full-spectrum (200–2500 nm) photocatalysis of halide

perovskites has almost never been reported.

Herein, we design an attractive photocatalytic system with excellent CO_2 emission reduction, which has favorable stability and can effectively absorb light energy in near infrared band to promote photocatalytic CO_2 reduction reaction. Natural soy lecithin was used as a ligand to construct Cs_2CuCl_4 MCs, which can adjust the morphology, particle size, crystal face and electronic structure of active phase, and maintain the colloidal and structural integrity of microcrystals over long-term in a large concentration range compared with conventional Cs_2CuCl_4 MCs. Under natural sunlight, full spectrum light (200–2500 nm) is absorbed by Cs_2CuCl_4 and SL-Cs_2CuCl_4 MCs photocatalysts. Ligand modification and full spectrum absorption enhance the photocatalytic behavior of CO_2 conversion to CO, and the CO conversion rate is increased by 5 times, which proves that the active phase tailoring and near-infrared light absorption have important effects on the photocatalytic CO_2 reduction performance. The chemical reaction path and active species were revealed by in-situ Fourier transform infrared (FT-IR), electron spin resonance (ESR), X-ray photoelectron (XPS) and density functional theory (DFT) spectroscopies. The results of DFT calculation show that the photocatalytic reduction of CO_2 to CO by Cs_2CuCl_4 is proposed to involve the concerted action of both Cs and Cu sites.

2. Experimental section

2.1. Synthesis of the Cs_2CuCl_4 MCs and SL-Cs_2CuCl_4 MCs

Cs_2CuCl_4 MCs were synthesized by dissolving 336.7 mg of CsCl (2.0 mmol) and 134.4 mg of $CuCl_2$ (1.0 mmol) in 2 mL of dimethyl sulfoxide to form a uniform precursor solution. The precursor solution was added to 10 mL of isopropyl alcohol under rapid and uniform stirring, and the reaction was completed within 2 minutes. Subsequently, the obtained mixed solution was centrifuged to remove the supernatant, and then precipitate is collected and washed with isopropyl alcohol
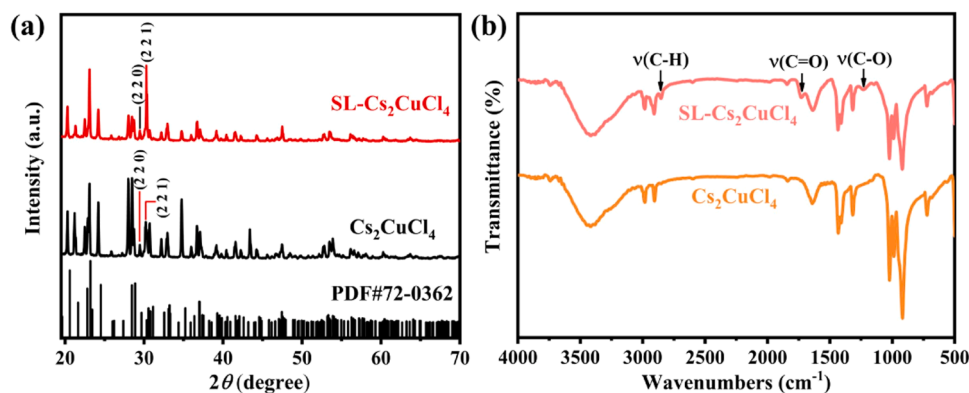
Fig. 2. (a) XRD patterns of Cs_2CuCl_4 and SL-Cs_2CuCl_4 MCs. (b) FT-IR spectra of Cs_2CuCl_4 and SL-Cs_2CuCl_4 MCs.

three times at 10,000 rpm. Finally, the Cs_2CuCl_4 MCs were obtained by vacuum drying at 60 °C for 24 hours. The synthesis of SL-Cs_2CuCl_4 MCs only needs to add soybean lecithin at the same time when the precursor solution was formed, and other procedures were the same as the synthesis of Cs_2CuCl_4 MCs.

2.2. Photocatalytic CO_2 reduction

The test was performed on the Labsolar-6A system (Perfect Light Co., China). The photocatalytic CO reduction system consists of a fully-enclosed quartzose reactor, a 300 W Xe lamp and gas chromatography (GC). Prior to catalysis, the 300 W Xe lamp (PLS-SXE300, Beijing Prefect Light) was configured for sunlight irradiation and the UV-Vis-NIR light source was obtained by a 300 W Xe lamp equipped with an optical filter (200–2500 nm). In a typical experiment, the 3 mg photocatalyst sample was ultrasonically dispersed in 1.0 mL isopropyl alcohol. Subsequently, the mixture solution was uniformly dropped on the glass piece (1.69*1.69 cm) and heated to 60 °C in an ambient atmosphere for 2 hours to remove the extraneous isopropyl alcohol to obtain the test sample. Finally, the treated glass piece was placed in 100 mL sealed Pyrex glass bottle with air removed by repeated washing, followed by CO_2 and 20 μL water, and the reaction pressure was 85 kPa~90 kPa.

3. Results and discussion

3.1. Synthesis and structural characterization

The Cs_2CuCl_4 and SL-Cs_2CuCl_4 MCs were synthesized by antisolvent method. As shown in Fig. 1a, b, the field emission scanning electron microscope (SEM) image shows that the microcrystalline size was significantly reduced after the addition of ligand lecithin, and it could be

seen from particle size analysis that the microcrystalline size was reduced from 7.22 μm to 3.32 μm. With the decrease of particle size, the Brunauer-Emmett-Teller (BET) surface area increased significantly from 0.3413 m^2/g to 1.4774 m^2/g, which helped to expose more active sites in the material, thereby improving the photocatalytic performance. To investigate whether the addition of ligands affects the microstructure of Cs_2CuCl_4 MCs, we studied the lattice streaks of Cs_2CuCl_4 MCs and SL-Cs_2CuCl_4 MCs using micrographs obtained by high-resolution transmission electron microscopy (HRTEM) (Fig. 1e, f). HRTEM images show high crystallinity, where lattice spacing of 0.294 nm, 0.427 nm, 0.291 nm and 0.297 nm can be clearly identified corresponding to the (104), (112), (221) and (220) crystal faces of Cs_2CuCl_4 MCs. The lattice spacing of 0.301 nm, 0.427 nm and 0.419 nm corresponds to the (220), (112) and (210) crystal faces of SL-Cs_2CuCl_4 MCs, respectively. The energy-dispersive X-ray spectroscopy (EDS) of Fig. 1g-l further confirmed that representative elements (i.e. Cs, Cu, Cl) were evenly distributed in Cs_2CuCl_4 MCs and SL-Cs_2CuCl_4 MCs.

The phases of the prepared microcrystal were characterized by powder X-ray diffraction (XRD). Fig. 2a shows the XRD curves of Cs_2CuCl_4 and SL-Cs_2CuCl_4 MCs. The diffraction peaks of each sample are very consistent with the standard monoclinic phase of Cs_2CuCl_4 (JCPDS No. 72–0362), indicating the high phase and component purity of the prepared Cs_2CuCl_4 MCs and SL-Cs_2CuCl_4 MCs. Interestingly, we observed a variation in the intensity of diffraction peaks, notably the (221) plane, subsequent to the ligand modification. This phenomenon could potentially be attributed to subtle alterations in the lattice structure upon the introduction of the lecithin ligand into Cs_2CuCl_4. These subtle changes might influence the crystal structure of Cs_2CuCl_4, consequently impacting the strength of the diffraction peaks. The effectiveness of ligand addition was studied by Fourier transform-infrared spectra (FT-IR) and nuclear magnetic resonance (NMR). As
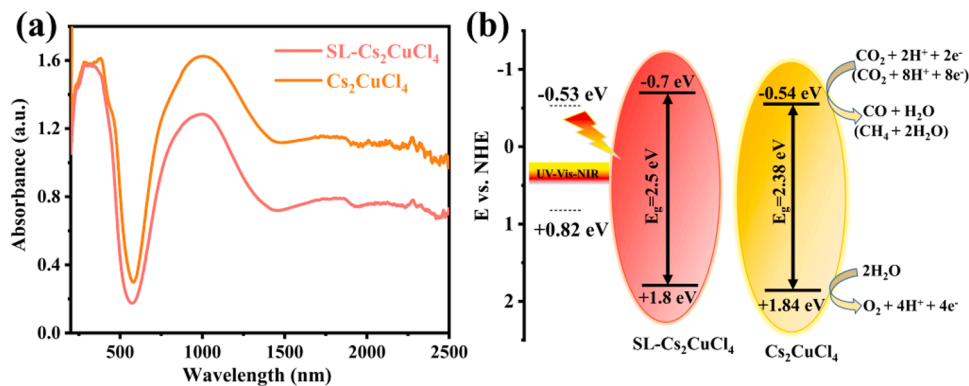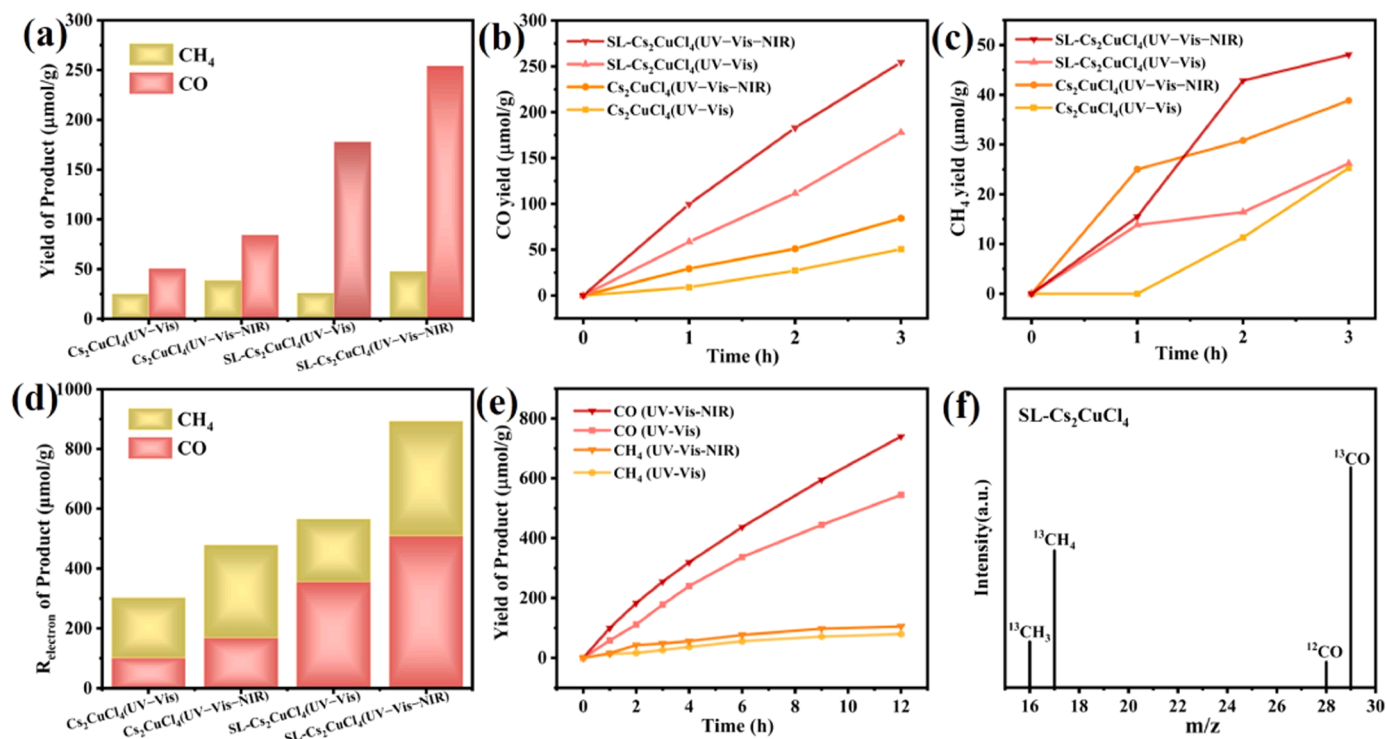

Fig. 3. (a) UV-Vis-NIR absorption spectra of Cs_2CuCl_4 and SL-Cs_2CuCl_4 MCs. (b) Band structures of Cs_2CuCl_4 and SL-Cs_2CuCl_4 MCs derived from the Tauc plots and XPS valence band spectra.

Fig. 4. (a) Comparison of photocatalytic CO_2 reduction performance of the prepared Cs_2CuCl_4 and SL-Cs_2CuCl_4 MCs. The time course of evolution on (b) CO and (c) CH_4 of Cs_2CuCl_4 and SL-Cs_2CuCl_4 MCs. (d) Photocatalytic electron consumption rate using the Cs_2CuCl_4 and SL-Cs_2CuCl_4 MCs as the photocatalysts. (e) Photocatalytic stability measurement of the SL-Cs_2CuCl_4 MCs. (f) Mass spectrometry spectra of $^{13}CO_2$ isotope experiments in the presence of SL-Cs_2CuCl_4 MCs.

depicted in Fig. 2b, three bands assigned to C-H, C=O and C-O vibrations appear at 2856, 1728 and 1226 cm^{-1},[16,21,32,33] respectively, which indicate the coexistence of lecithin on the surface of the Cs_2CuCl_4 MCs. The effective binding of Cs_2CuCl_4 to ligand was also directly confirmed by ^1H NMR spectra (Fig. S1).

In order to study the surface chemical states of Cs_2CuCl_4 and SL-Cs_2CuCl_4, X-ray photoelectron spectroscopy (XPS) tests were performed. The XPS survey spectrum (Fig. S2a) confirms the presence of Cs, Cu, and Cl elements. Fig. S2b-d show the high-resolution XPS (HRXPS) spectra of Cs 3d, Cu 2p, and Cl 2p for the Cs_2CuCl_4 and SL-Cs_2CuCl_4 MCs powder sample. The HRXPS spectra shows that the peaks of Cs 3d and Cl 2d remain basically unchanged after the addition of ligand lecithin. The peaks of Cs 3d are 724.13 eV and 738.06 eV, corresponding to Cs $3d_{5/2}$ and $3d_{3/2}$[34]. Typical peaks are shown at 198.1 eV and 199.65 eV, which are attributed to the binding energies of Cl $2p_{1/2}$ and Cl $2p_{3/2}$[35], respectively. For Cs_2CuCl_4, two peaks detect by the high-resolution Cu2p XPS at 934.59 eV and 954.54 eV, as well as satellite peaks near 941 eV, 944 eV and 962 eV, can be attributed to Cu^{2+}, while two peaks measure at 932.1 eV and 951.9 eV can be attributed to Cu^+[36]. Each peak of SL-Cs_2CuCl_4 shows a red shift of about 0.37 eV, which means that the addition of ligands causes a change in the chemical state of the atoms on the Cs_2CuCl_4 MCs surface.

The amazing light absorption capacity of photocatalyst is the prerequisite for achieving excellent photocatalytic activity. Therefore, UV-Vis-NIR absorption spectra of Cs_2CuCl_4 and SL-Cs_2CuCl_4 MCs were recorded to evaluate their utilization of solar photons. As depicted in Fig. 3a, the UV-Vis-NIR absorption spectra of Cs_2CuCl_4 and SL-Cs_2CuCl_4 MCs were collected in the wavelength range from 200 nm to 2500 nm. Both Cs_2CuCl_4 and SL-Cs_2CuCl_4 MCs have strong absorption from the UV region to the NIR region, this can be attributed to the typical light absorption of Cu metals [37–39]. The corresponding Tauc plots of Cs_2CuCl_4 and SL-Cs_2CuCl_4 MCs are presented in Fig. S3a, b, and the bandgaps (E_g) of Cs_2CuCl_4 and SL-Cs_2CuCl_4 MCs are found to 2.38 eV and 2.5 eV, respectively. The difference in bandgaps may be due to the

slight effect of lecithin on the electronic structure of Cs_2CuCl_4 MCs and the reduction of particle size due to the addition of ligands. The valence band edge potentials (V_{VB}) were further derived from the XPS valence band spectra of Cs_2CuCl_4 and SL-Cs_2CuCl_4 MCs (Fig. S3c, d), with values of 1.84 eV and 1.8 eV, respectively. Based on E_g and V_{VB} values, the corresponding conduction edge potentials (V_{CB}) of Cs_2CuCl_4 and SL-Cs_2CuCl_4 MCs are derived as −0.54 eV and −0.7 eV. According to the above results, Cs_2CuCl_4 and SL-Cs_2CuCl_4 MCs band structures are obtained (Fig. 3b).

3.2. Photocatalytic CO_2 reduction with concentrated solar irradiation for Cs_2CuCl_4 and SL-Cs_2CuCl_4 MCs

Inspired by the unique photoelectric properties of Cs_2CuCl_4 and SL-Cs_2CuCl_4 MCs, a series of photocatalytic CO_2 reduction reactions were performed to verify their potential as photocatalysts. As shown in Fig. 4, the photocatalytic activities of Cs_2CuCl_4 and SL-Cs_2CuCl_4 MCs under UV-Vis and UV-Vis-NIR light were investigated and compared. By monitoring, CO was the main product in all the photocatalysts. After 3 hours of UV-Vis irradiation, the CO and CH_4 yields of Cs_2CuCl_4 were 50.59 μmol g^{-1} and 25.29 μmol g^{-1}, respectively, while the CO and CH_4 yields of SL-Cs_2CuCl_4 were increased to 178 μmol g^{-1} and 26.19 μmol g^{-1}, which is consistent with the previous SEM and BET analysis results. The selectivity of CO products increased from 66% to 87% with the introduction of ligand lecithin. After 3 hours of UV-Vis-NIR light irradiation, the CO and CH_4 yields of Cs_2CuCl_4 were 84.38 μmol g^{-1} and 38.83 μmol g^{-1}, respectively, while the yields of SL-Cs_2CuCl_4 were increased to 254.46 μmol g^{-1} and 48.06 μmol g^{-1} under the same conditions (Fig. 4a-c). Subsequently, the monitoring of O_2 evolution during the photocatalytic reaction was performed to verify the CO_2 reduction by H_2O (Fig. S4a, b). As expected, SL-Cs_2CuCl_4 showed the highest O_2 yield during the photocatalytic reaction under UV-Vis-NIR illumination. The above proves that Cs_2CuCl_4 and SL-Cs_2CuCl_4 MCs can utilize more photons from the solar spectrum and promote

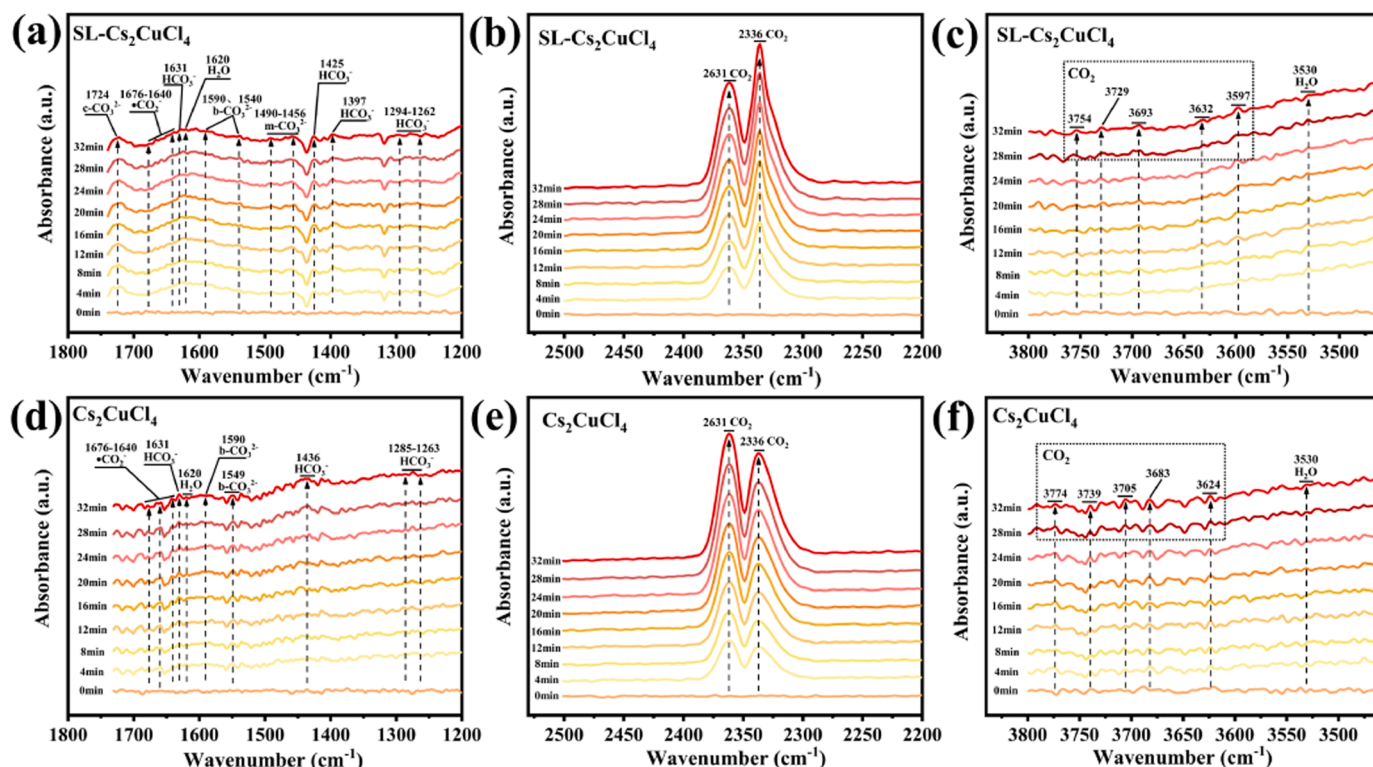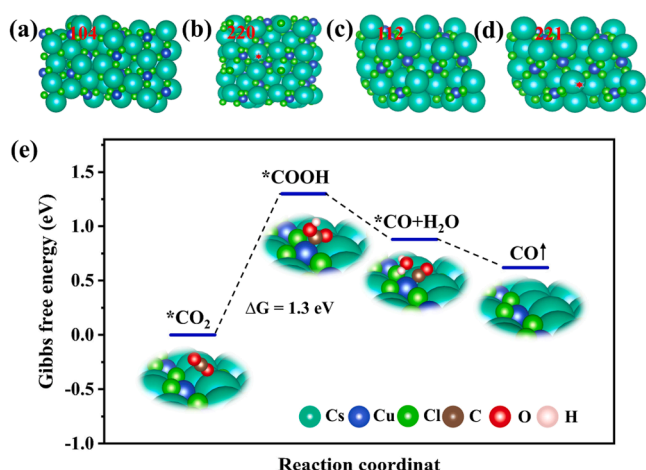**Fig. 5.** In-situ FT-IR tests for CO_2 and H_2O interaction with SL-Cs_2CuCl_4 MCs (a-c) and Cs_2CuCl_4 MCs (d-f) in the dark.

photocatalytic performance. This observation confirms that Cs_2CuCl_4 and SL-Cs_2CuCl_4 MCs can be used as a full-spectrum (covering the entire solar spectrum from 200 to 2500 nm) photocatalyst. The selectivity of CO products increased from 68% of Cs_2CuCl_4 to 84% of SL-Cs_2CuCl_4, indicating that the modification of ligands significantly improved the selectivity of CO products. In order to further evaluate the reducing capacity of Cs_2CuCl_4 and SL-Cs_2CuCl_4 MCs under UV-Vis and UV-Vis-NIR irradiation, the electron consumption during the reduction process was calculated. The formula $R_{electron} = R (CO) \times 2 + R (CH_4) \times 8$ is used to obtain the electron consumption of Cs_2CuCl_4 and SL-Cs_2CuCl_4 MCs, where R (CO) and R (CH_4) are the CO and CH_4 yields, respectively. As shown in Fig. 4d, the highest electron consumption rate of SL-Cs_2CuCl_4 MCs under UV-Vis-NIR irradiation was 893.4 μmol g^{-1}, indicating the best performance of photocatalytic CO_2 reduction. In addition, the durability of SL-Cs_2CuCl_4 MCs in the photocatalytic reaction was performed in a 12-hour cycle. Fig. 4e shows the time-dependent CO and CH_4 yields of SL-Cs_2CuCl_4 MCs under UV-Vis and UV-Vis-NIR irradiation as a photocatalyst. After 12 hours of continuous irradiation, the gas formation rate did not decrease significantly, which further proves that SL-Cs_2CuCl_4 MCs have good stability. In order to determine the carbon source of gaseous products, $^{13}CO_2$ was used as the carbon source for isotope labeling experiments. As shown in Fig. 4f, two strong signals of ^{13}CO ($m/z = 29$) and $^{13}CH_4$ ($m/z = 17$) can be clearly detected, which strongly proves that these reducing products are derived from the CO_2 photoreduction reaction.

To demonstrate the stability of the catalyst, Cs_2CuCl_4 and SL-Cs_2CuCl_4 MCs were characterized by thermogravimetric analysis (TGA). As shown in Fig. S5a, Cs_2CuCl_4 and SL-Cs_2CuCl_4 MCs are decomposed slightly at around 120 °C. Cs_2CuCl_4 MCs was decomposed for the second time at about 450 °C, but SL-Cs_2CuCl_4 MCs was decomposed for the second time at about 650 °C, indicating that the addition of ligand lecithin can enhance the stability of microcrystals. In order to further demonstrate the stability of the catalyst, the crystal structure of SL-Cs_2CuCl_4 MCs before and after photocatalysis was characterized. As shown in Fig. S5b, the XRD pattern of SL-Cs_2CuCl_4 MCs did not show

significant changes before and after the photocatalytic test, which proves that SL-Cs_2CuCl_4 MCs has relatively favorable stability. Additionally, the stability of Cs_2CuCl_4 and SL-Cs_2CuCl_4 MCs was tested after being stored at 100 °C for 120 hours and irradiated at 365 nm ultraviolet lamp for 120 hours. XRD test results are shown in Fig. S5c, d. The XRD patterns of Cs_2CuCl_4 and SL-Cs_2CuCl_4 MCs treated by the two methods are basically consistent with the original XRD patterns. This shows that Cs_2CuCl_4 and SL-Cs_2CuCl_4 MCs do not undergo significant phase transition after treatment with these two methods. The above results show that Cs_2CuCl_4 and SL-Cs_2CuCl_4 MCs have relatively good thermal and optical stability.

Charge transfer and separation play a crucial role in photocatalytic redox reactions. The effect of lecithin addition on the photoluminescence kinetics of Cs_2CuCl_4 MCs was further studied by time-resolved photoluminescence (TRPL) spectral test, and the TRPL curve was fitted by single exponential method. As shown in Fig. S6a, b, the average lifetime (τ_{av}) of Cs_2CuCl_4 and SL-Cs_2CuCl_4 MCs were 106.85 μs and 110.61 μs, respectively, indicating that the addition of ligands slightly promotes charge transfer and surface redox reactions. In addition, as shown in Fig. S6c, photoelectric chemical experiments further demonstrate the charge separation process in SL-Cs_2CuCl_4 MCs. The photocurrent density of SL-Cs_2CuCl_4 MCs (about 30 μA cm^{-2}) is higher than that of Cs_2CuCl_4 MCs (about 14 μA cm^{-2}), which strongly indicates the enhanced photoinduced charge carrier separation efficiency in SL-Cs_2CuCl_4 MCs. At the same time, the charge transport behavior of the two electrodes was further detected by electrochemical impedance spectra (EIS). Nyquist diagram illustrates that the resistance of charge transfer SL-Cs_2CuCl_4 MCs decreases compared to Cs_2CuCl_4 MCs (Fig. S6d). The above data show that the addition of ligand lecithin can effectively inhibit charge recombination and promote charge separation in Cs_2CuCl_4 MCs photocatalyst. This may be related to the morphological changes after the addition of ligands. Convincingly, these results confirm that the addition of ligand lecithin is advantageous for photocatalytic CO_2 reduction.
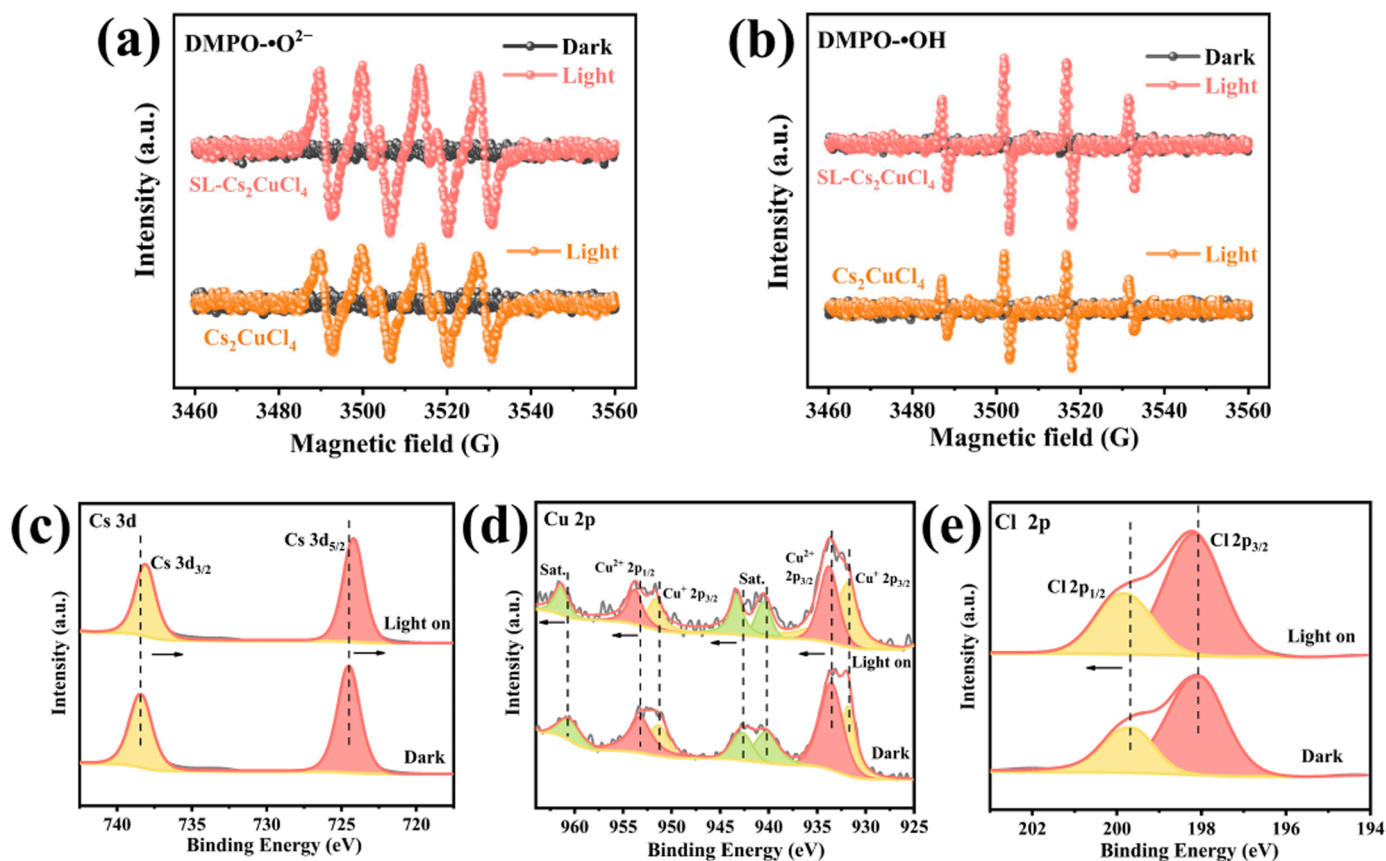
Fig. 6. In-situ FT-IR tests of CO_2 and H_2O interaction with SL-Cs_2CuCl_4 MCs (a, b) and Cs_2CuCl_4 MCs (c, d) under constant 300 W Xe lamp illumination.

3.3. Photocatalytic reduction mechanism

To further understand the photocatalytic reduction reaction path of CO_2 on catalysts, we performed in-situ FT-IR spectroscopy tests to accurately track the reaction intermediates during the surface adsorption, activation, and transformation of CO_2 on Cs_2CuCl_4 and SL-Cs_2CuCl_4 MCs. Fig. 5 illustrates the surface species produced by Cs_2CuCl_4 and SL-Cs_2CuCl_4 MCs after absorbing CO_2 and H_2O in the dark. The adsorption peaks at $1640 \sim 1676$ cm^{-1} are attributed to the characteristic vibration pattern of $\bullet CO_2^-$[40,41], which is considered to be an important surface species for hydrogenation of CO_2 to obtain CO products. The strong peaks at 2336 and 2631 cm^{-1} are attributed to the asymmetric stretching of CO_2[1,42], which highlights the good adsorption capacity of Cs_2CuCl_4 and SL-Cs_2CuCl_4 MCs for CO_2. It can be seen from Fig. 5b, e that the peak of SL-Cs_2CuCl_4 MCs is higher than Cs_2CuCl_4 MCs, which is consistent with the addition of ligand lecithin that can provide more active sites for CO_2 adsorption. Adsorbed CO_2 was also detected near 3632 and 3739 cm^{-1}. The vibration band at 3530 cm^{-1} belongs to the stretching vibration of the OH$^-$ bond in H_2O[43]. The apparent peak at 1620 cm^{-1} indicates effective adsorption of H_2O[31]. The peaks of Cs_2CuCl_4 MCs at 1549 and 1590 cm^{-1} are attributed to the bicentate carbonate species (b-CO_3^{2-}). And SL-Cs_2CuCl_4 MCs showed more carbonate species, peaks at 1540 and 1590 cm^{-1} correspond to bicentate carbonate species (b-CO_3^{2-}), peaks at 1456–1490 cm^{-1} belong to monodontic carbonate (m-CO_3^{2-}), and peaks at 1724 cm^{-1} correspond to

chelating-bridged carbonate (c-CO_3^{2-})[31,44,45]. The presence of various carbonate species can be attributed to the formation of carbonic acid and/or the adsorbed CO_2 on the surface of the catalyst. Moreover , bands at 1262–1294, 1397, 1425,1436 and 1631 cm^{-1} can correspond to bicarbonate (HCO_3^-)[31,45,46], which is caused by the surface interaction of adsorbed CO_2 and H_2O. All observed carbonate and bicarbonate species are important intermediates involved in CO_2 photo-conversion, and HCO_3^- plays a key role in the process of CO_2 conversion to CO, and the HCO_3^- peak on Cs_2CuCl_4 and SL-Cs_2CuCl_4 MCs also predict the production of primary CO.

Fig. 6 shows the in-situ FT-IR spectra of Cs_2CuCl_4 and SL-Cs_2CuCl_4 MCs collected every 4 min under irradiation in CO_2 and H_2O. Obviously, positive and negative peaks can be clearly observed during the photocatalytic reaction, which correspond to species formation and depletion respectively. The negative peaks of carbonate species CO_3^{2-} (1590, 1540, 1464, 1457, 1377,1320 and 1319 cm^{-1}) and HCO_3^- (1436, 1406 and 1305 cm^{-1})[31,40,46,47], confirmed that the adsorbed and activated species were consumed and immediately converted during irradiation of SL-Cs_2CuCl_4 and Cs_2CuCl_4 (Fig. 6a, c) , and it was evident that ligand lecithin modified Cs_2CuCl_4 had a higher peak, indicating that more CO_2 was consumed and converted. The positive peaks of *COOH (1743, 1573, 1567, 1565 and 1550 cm^{-1})[46,48,49], CO* (1719 and1709 cm^{-1}), and $\bullet CO_2^-$ (1690 and 1630 cm^{-1})[31,50] appeared and increased in intensity as the photocatalytic reaction continued. The detection of *COOH and CO* confirmed that illumination of SL-Cs_2CuCl_4 and

Fig. 7. (a-d) Crystal plane structure of Cs_2CuCl_4 (104), (220), (112) and (221). (e) Gibbs free energy diagrams of CO_2 reduction reaction to CO on Cs_2CuCl_4(220) surface. The inserts represent reaction intermediates.

Cs_2CuCl_4 MCs led to the formation of CO by multistep hydrogenation of $\bullet CO_2^-$ radicals. Moreover, the increase of peak intensity of SL-Cs2CuCl4 was more obvious, which may be one of the significant reasons for the increased selectivity of CO products caused by ligand modification. Additionally, the high-wavenumber region of SL-Cs_2CuCl_4 and Cs_2CuCl_4 MCs spectra confirms the formation of a variety of reaction intermediates, including CH$_3$O* (2833 cm^{-1}), CH$_3$* (2900 and 2954 cm^{-1}), and CH$_2$*(2932, 2930, 2927, 2912, 2878 and 2854 cm^{-1}) [31,51–53] (Fig. 6b, d). The key CH$_x$* species detected indicate CH$_4$ formation on the surface of SL-Cs_2CuCl_4 and Cs_2CuCl_4 MCs. It is worth

noting that these peak intensifies of the reaction intermediates and products gradually increase with the extension of irradiation time, indicating that the photocatalytic reaction is continuous.

Theoretical calculations based on DFT were employed to investigate the mechanism behind the high selectivity of CO over the (220) facet of Cs_2CuCl_4. The structure of various crystal faces (Fig. 7a-d), including (104), (112), (220), and (221), was examined, revealing that (104) and (112) faces were ineffective in capturing CO_2 molecules. However, on the (220) and (221) surfaces, CO_2 molecules attached to Cs atoms, with calculated CO_2 adsorption energies of -0.37 and -0.33 eV, respectively. Further exploration focused on the protonation process of adsorbed CO_2. Unexpectedly, initial attempts at protonation on the (221) surface failed, as the H atom was unable to bond with the O atom. Conversely, protonation of CO_2 on the (220) surface proceeded smoothly, resulting in the formation of CO. Drawing on these DFT calculations, a proposed reaction pathway for CO_2 photoreduction was developed, as depicted in Fig. 7e. Initially, the O end of the CO_2 molecule binds to a Cs atomic site. Upon the first protonation, a *COOH intermediate forms and attaches to the adjacent Cu atom. Subsequent stages involve further protonation to generate *CO intermediates, accompanied by the release of H_2O molecules. Desorption of H_2O molecules, followed by *CO desorption, ultimately leads to CO formation. The hindrance to CO_2 protonation on the (221) surface is attributed to the spatial separation between Cu and Cs sites, making collaboration between the two sites unfeasible. Consequently, the photocatalytic reduction of CO_2 to CO facilitated by Cs_2CuCl_4 is proposed to involve the concerted action of both Cs and Cu sites.

The in-situ electron spin resonance (ESR) spectroscopy was used to monitor the DMPO-$\bullet O^{2-}$ and DMPO-$\bullet OH$ changes in Cs_2CuCl_4 and SL-Cs_2CuCl_4 MCs before and after irradiation (Fig. 8a-b). In the dark, hardly any distinct characteristic peaks were observed, meaning that Cs_2CuCl_4

Fig. 8. The in-situ ESR profiles for (a) DMPO-$\bullet O^{2-}$ and (b) DMPO-$\bullet OH$ for Cs_2CuCl_4 MCs and SL-Cs_2CuCl_4 MCs. The in-situ high-resolution XPS spectrum of SL-Cs_2CuCl_4 MCs: (c) Cs 3d, (d) Cu 2p and (e) Cl 2p.

and SL-Cs_2CuCl_4 MCs produced little or no $\bullet O^{2-}$ or $\bullet OH$ species in the absence of light. However, a clear signal was observed on the sample under visible light irradiation, and the signal strength of superoxide and hydroxyl radicals in SL-Cs_2CuCl_4 MCs was significantly stronger than that of Cs_2CuCl_4 MCs, indicating that e^- and h^+ were excited, which was consistent with photocatalytic activity. The above results confirm that the addition of ligand lecithin inhibits charge recombination and makes the photoexcited carrier better separated.

In situ XPS spectroscopy was performed to evaluate the charge transfer behavior of SL-Cs_2CuCl_4 under light irradiation (Fig. 8c-e). After the lights are turned off, the peaks of Cs 2p, Cu 2p, and Cl 3d all shift accordingly. The change of binding energy is the result of the transfer of photogenerated electrons under irradiation, and the decrease and increase of binding energy can be attributed to the obtain and loss of electrons [5,54,55]. Notably, compared to the fine spectrum of SL-Cs_2CuCl_4 MCs in the dark, the binding energies of Cl 2p and Cu 2p shift significantly to higher energy levels under light, while the binding energies of Cs 3d shift to lower energy levels. This indicates the resulting electron transfer from Cl 2p and Cu 2p towards Cs 3d.

4. Conclusions

In summary, we have developed a metal halide perovskite Cs_2CuCl_4 MCs photocatalyst with significant light absorption in UV, Vis and NIR light, using the antisolvent method. The introduction of ligands increases the active site density, exposes highly active crystal planes and optimizes the electronic structure, which improves the photoreduction performance of CO_2 by nearly 5 times, which was significantly better than the original Cs_2CuCl_4 MCs. Meanwhile, the photocatalytic activity under UV-Vis and UV-Vis-NIR light was compared, and the photocatalytic performance was significantly improved under the full spectrum. And active phase and photocatalytic reaction mechanism were clearly elucidated by a series of in situ characterization technologies such as XPS, ESR and FT-IR. Combined with DFT calculation, it was confirmed that the photocatalytic reduction of CO_2 to CO by Cs_2CuCl_4 was caused by the synergistic action of Cs and Cu sites. This study provides a new perspective for constructing full spectral responses based on halide perovskites to enhance photocatalytic CO_2 reduction.

CRediT authorship contribution statement

Yichen Liu: Methodology. **Wei Chen:** Formal analysis, Investigation. **Fan Dong:** Resources. **Hao Ma:** Validation. **Liqin Gao:** Resources. **Zhiqiong Luo:** Investigation. **Faling Ling:** Validation. **Faguang Kuang:** Visualization. **Hongmei Ran:** Methodology, Formal analysis, Data curation, Writing – original draft. **Min Mo:** Resources. **Xiaosheng Tang:** Writing – review & editing, Supervision, Funding acquisition, Conceptualization. **Junan Lai:** Supervision. **Heng Luo:** Validation. **Qian Zhang:** Resources. **Baofei Sun:** Validation, Supervision, Resources, Methodology. **Jinchen Zhou:** Validation. **Bo Gao:** Investigation. **Daofu Wu:** Writing – review & editing, Supervision, Funding acquisition, Conceptualization.

Declaration of Competing Interest

The authors declare that they have no known competing financial interests or personal relationships that could have appeared to influence the work reported in this paper

Data availability

Data will be made available on request.

Acknowledgments

Appendix A. Supporting information

Supplementary data associated with this article can be found in the online version at doi:10.1016/j.apcatb.2024.124048.

References

[1] Z. Li, G. Zhu, W. Zhang, L. Zhu, B. Cao, J. Gao, X. Shi, Y. Huang, P. Liu, M. Hojamberdiev, Dual-functional copper (Cu^0/Cu^{2+})-modified $SrTiO_{3-\delta}$ nanosheets with enhanced photothermal catalytic performance for CO_2 reduction and H_2 evolution, Chem. Eng. J. 452 (2023) 139378.

[2] E. Gong, S. Ali, C.B. Hiragond, H.S. Kim, N.S. Powar, D. Kim, H. Kim, S.-I. In, Solar fuels: research and development strategies to accelerate photocatalytic CO_2 conversion into hydrocarbon fuels, Energy Environ. Sci. 15 (2022) 880–937.

[3] V. Andrei, G.M. Ucoski, C. Pornrungroj, C. Uswachoke, Q. Wang, D.S. Achilleos, H. Kasap, K.P. Sokol, R.A. Jagt, H. Lu, T. Lawson, A. Wagner, S.D. Pike, D. S. Wright, R.L.Z. Hoye, J.L. MacManus-Driscoll, H.J. Joyce, R.H. Friend, E. Reisner, Floating perovskite-$BiVO_4$ devices for scalable solar fuel production, Nature 608 (2022) 518–522.

[4] Y. Sun, J. Xie, Z. Fu, H. Zhang, Y. Yao, Y. Zhou, X. Wang, S. Wang, X. Gao, Z. Tang, S. Li, X. Wang, K. Nie, Z. Yang, Y.M. Yan, Boosting CO_2 Electroreduction to C_2H_4 via Unconventional Hybridization: High-Order Ce^{4+} 4f and O 2p Interaction in Ce-Cu_2O for Stabilizing Cu^+, ACS Nano 17 (2023) 13974–13984.

[5] Z. Liu, J. Liang, Q. Song, Y. Li, Z. Zhang, M. Zhou, W. Wei, H. Xu, C.-S. Lee, H. Li, Z. Jiang, Construction atomic-level N-P charge transfer channel for boosted CO_2 photoreduction, Appl. Catal. B: Environ. 328 (2023) 122472.

[6] F. Wang, R. Fang, X. Zhao, X.P. Kong, T. Hou, K. Shen, Y. Li, Ultrathin Nanosheet Assembled Multishelled Superstructures for Photocatalytic CO_2 Reduction, ACS Nano 16 (2022) 4517–4527.

[7] Q. Zhang, J. Wang, F. Guo, G. He, X. Yang, W. Li, J. Xu, Z. Yin, Nitrogen cold plasma treatment stabilizes Cu^0/Cu^+ electrocatalysts to enhance CO_2 to C2 conversion, J. Energy Chem. 84 (2023) 321–328.

[8] Q. Wang, C. Pornrungroj, S. Linley, E. Reisner, Strategies to improve light utilization in solar fuel synthesis, Nat. Energy 7 (2021) 13–24.

[9] G. Jia, M. Sun, Y. Wang, Y. Shi, L. Zhang, X. Cui, B. Huang, J.C. Yu, Asymmetric Coupled Dual-Atom Sites for Selective Photoreduction of Carbon Dioxide to Acetic Acid, Adv. Funct. Mater. 32 (2022) 2206817.

[10] Y. Liu, F. Wang, Z. Jiao, S. Bai, H. Qiu, L. Guo, Photochemical systems for solar-to-fuel production, Electrochem. Energy Rev. 5 (2022) 5.

[11] J. Li, N. Arif, T. Lv, H. Fang, X. Hu, Y.J. Zeng, Towards Full-spectrum Photocatalysis: Extending the Near-infrared Region, ChemCatChem 14 (2022) e202200361.

[12] D. Mateo, N. Morlanes, P. Maity, G. Shterk, O.F. Mohammed, J. Gascon, Efficient visible-light driven photothermal conversion of CO_2 to methane by nickel nanoparticles supported on barium titanate, Adv. Funct. Mater. 31 (2020) 2008244.

[13] R. Verma, R. Belgamwar, P. Chatterjee, R. Bericat-Vadell, J. Sa, V. Polshettiwar, Nickel-Laden Dendritic Plasmonic Colloidosomes of Black Gold: Forced Plasmon Mediated Photocatalytic CO_2 Hydrogenation, ACS Nano 17 (2023) 4526–4538.

[14] Q.M. Sun, J.J. Xu, F.F. Tao, W. Ye, C. Zhou, J.H. He, J.M. Lu, Boosted Inner Surface Charge Transfer in Perovskite Nanodots@Mesoporous Titania Frameworks for Efficient and Selective Photocatalytic CO_2 Reduction to Methane, Angew. Chem., Int. Ed. 61 (2022) e202200872.

[15] M.S. Sena, J. Cui, Y. Baghdadi, E. Rattner, M. Daboczi, A.L. Lopes-Moriyama, A. G. dos Santos, S. Eslava, Lead-Free Halide Perovskite $Cs_2AgBiBr_6$/Bismuthene Composites for Improved CH_4 Production in Photocatalytic CO_2 Reduction, ACS Appl. Energy Mater. 6 (2023) 10193–10204.

[16] H. Wang, W. Lu, P. Xu, J. Luo, K. Yao, J. Zhang, X. Wei, S. Peng, H. Cheng, H. Hu, K. Sun, Highly Stable $CsPbBr_3$ Nanocrystals for Photocatalytic Reduction of CO_2: Ionic Liquid as a Surface Passivation Ligand and Reaction Precursor, ACS Sustain. Chem. Eng. 11 (2023) 5963–5972.

[17] T. Chen, M. Zhou, W. Chen, Y. Zhang, S. Ou, Y. Liu, $Cs_2AgInCl_6$ double perovskite quantum dots decorated with Ag nanoparticles for photocatalytic CO_2 reduction, Sustain. Energy Fuels 5 (2021) 3598–3605.

[18] M. Ahlawat, Neelakshi, R. Ramapanicker, V. Govind Rao, Design Principle of a Water-Dispersed Photocatalytic Perovskite through Ligand Deconstruction, ACS Energy Lett. 8 (2023) 2159–2168.

[19] S. Chen, H. Yin, P. Liu, Y. Wang, H. Zhao, Stabilization and Performance Enhancement Strategies for Halide Perovskite Photocatalysts, Adv. Mater. 35 (2023) e2203836.

[20] G. Jiang, C. Guhrenz, A. Kirch, L. Sonntag, C. Bauer, X. Fan, J. Wang, S. Reineke, N. Gaponik, A. Eychmuller, Highly Luminescent and Water-Resistant CsPbBr$_3$-CsPb$_2$Br$_5$ Perovskite Nanocrystals Coordinated with Partially Hydrolyzed Poly (methyl methacrylate) and Polyethylenimine, ACS Nano 13 (2019) 10386–10396.

[21] Z. Chen, Y. Hu, J. Wang, Q. Shen, Y. Zhang, C. Ding, Y. Bai, G. Jiang, Z. Li, N. Gaponik, Boosting Photocatalytic CO$_2$ Reduction on CsPbBr$_3$ Perovskite Nanocrystals by Immobilizing Metal Complexes, Chem. Mater. 32 (2020) 1517–1525.

[22] Y. Zhu, Y. Liu, K.A. Miller, H. Zhu, E. Egap, Lead Halide Perovskite Nanocrystals as Photocatalysts for PET-RAFT Polymerization under Visible and Near-Infrared Irradiation, ACS Macro Lett. 9 (2020) 725–730.

[23] X. Wang, B. Hu, Y. Li, G. Zhang, Lead-free halide perovskite photocatalysts for photocatalytic CO$_2$ reduction: a review, Sol. Rrl. 7 (2023) 2300410.

[24] J. Ye, M.M. Byranvand, C.O. Martinez, R.L.Z. Hoye, M. Saliba, L. Polavarapu, Defect Passivation in Lead-Halide Perovskite Nanocrystals and Thin Films: Toward Efficient LEDs and Solar Cells, Angew. Chem., Int. Ed. 60 (2021) 21636–21660.

[25] L.K. Ono, S.F. Liu, Y. Qi, Reducing Detrimental Defects for High-Performance Metal Halide Perovskite Solar Cells, Angew. Chem., Int. Ed. 59 (2020) 6676–6698.

[26] J. Wang, Y. Shi, Y. Wang, Z. Li, Rational Design of Metal Halide Perovskite Nanocrystals for Photocatalytic CO$_2$ Reduction: Recent Advances, Challenges, and Prospects, ACS Energy Lett. 7 (2022) 2043–2059.

[27] W. Huang, Q. Hua, T. Cao, Influence and Removal of Capping Ligands on Catalytic Colloidal Nanoparticles, Catal. Lett. 144 (2014) 1355–1369.

[28] Q. Hua, K. Chen, S. Chang, H. Bao, Y. Ma, Z. Jiang, W. Huang, Reduction of Cu$_2$O nanocrystals: reactant-dependent influence of capping ligands and coupling between adjacent crystal planes, RSC Adv. 1 (2011) 1200–1203.

[29] H.B. Zhao, J.F. Liao, Y. Teng, H.Y. Chen, D.B. Kuang, Inorganic copper-based halide perovskite for efficient photocatalytic CO$_2$ reduction, ACS Appl. Mater. Interfaces 14 (2022) 43354–43361.

[30] L. Yuan, S.-F. Hung, Z.-R. Tang, H.M. Chen, Y. Xiong, Y.-J. Xu, Dynamic Evolution of Atomically Dispersed Cu Species for CO$_2$ Photoreduction to Solar Fuels, ACS Catal. 9 (2019) 4824–4833.

[31] J. Sheng, Y. He, M. Huang, C. Yuan, S. Wang, F. Dong, Frustrated Lewis Pair Sites Boosting CO$_2$ Photoreduction on Cs$_2$CuBr$_4$ Perovskite Quantum Dots, ACS Catal. 12 (2022) 2915–2926.

[32] L. Wu, Q. Zhong, D. Yang, M. Chen, H. Hu, Q. Pan, H. Liu, M. Cao, Y. Xu, B. Sun, Q. Zhang, Improving the Stability and Size Tunability of Cesium Lead Halide Perovskite Nanocrystals Using Trioctylphosphine Oxide as the Capping Ligand, Langmuir 33 (2017) 12689–12696.

[33] Q. Wu, J. Cao, X. Wang, Y. Liu, Y. Zhao, H. Wang, Y. Liu, H. Huang, F. Liao, M. Shao, Z. Kang, A metal-free photocatalyst for highly efficient hydrogen peroxide photoproduction in real seawater, Nat. Commun. 12 (2021) 483.

[34] B. Xie, D. Chen, N. Li, Q. Xu, H. Li, J. Lu, Lead-Free Cs$_3$Bi$_2$Br$_9$ perovskite In-situ growth on 3D Flower-like g-C$_3$N$_4$ microspheres to improve photocatalytic performance, Chem. Eng. J. 452 (2023) 139662.

[35] X. Shi, Xa Dong, Y. He, P. Yan, S. Zhang, F. Dong, Photoswitchable Chlorine Vacancies in Ultrathin Bi$_4$O$_5$Cl$_2$ for Selective CO$_2$ Photoreduction, ACS Catal. 12 (2022) 3965–3973.

[36] Z. Lyu, S. Zhu, M. Xie, Y. Zhang, Z. Chen, R. Chen, M. Tian, M. Chi, M. Shao, Y. Xia, Controlling the Surface Oxidation of Cu Nanowires Improves Their Catalytic Selectivity and Stability toward C$_{2+}$ Products in CO$_2$ Reduction, Angew. Chem., Int. Ed. 60 (2021) 1909–1915.

[37] L. Cheng, H. Yin, C. Cai, J. Fan, Q. Xiang, Single Ni Atoms Anchored on Porous Few-Layer g-C$_3$N$_4$ for Photocatalytic CO$_2$ Reduction: The Role of Edge Confinement, Small 16 (2020) e2002411.

[38] G. Shi, L. Yang, Z. Liu, X. Chen, J. Zhou, Y. Yu, Photocatalytic reduction of CO$_2$ to CO over copper decorated g-C$_3$N$_4$ nanosheets with enhanced yield and selectivity, Appl. Surf. Sci. 427 (2018) 1165–1173.

[39] D.-E. Lee, S. Moru, R. Bhosale, W.-K. Jo, S. Tonda, Cu–Ni core–shell bimetallic cocatalyst decorated polymeric carbon nitride for highly efficient and selective methane production from photocatalytic CO$_2$ reduction, Appl. Surf. Sci. 599 (2022) 153973.

[40] M. Wang, M. Shen, X. Jin, J. Tian, M. Li, Y. Zhou, L. Zhang, Y. Li, J. Shi, Oxygen Vacancy Generation and Stabilization in CeO$_{2-x}$ by Cu Introduction with Improved CO$_2$ Photocatalytic Reduction Activity, ACS Catal. 9 (2019) 4573–4581.

[41] J. Wu, X. Li, W. Shi, P. Ling, Y. Sun, X. Jiao, S. Gao, L. Liang, J. Xu, W. Yan, C. Wang, Y. Xie, Efficient Visible-Light-Driven CO$_2$ Reduction Mediated by Defect-Engineered BiOBr Atomic Layers, Angew. Chem., Int. Ed. 57 (2018) 8719–8723.

[42] Y. Zhang, L. Cao, G. Bai, X. Lan, Engineering Single Cu Sites into Covalent Organic Framework for Selective Photocatalytic CO$_2$ Reduction, Small 19 (2023) 2300035.

[43] X. Ren, M. Gao, Y. Zhang, Z. Zhang, X. Cao, B. Wang, X. Wang, Photocatalytic reduction of CO2 on BiOX : Effect of halogen element type and surface oxygen vacancy mediated mechanism, Appl. Catal., B 274 (2020) 119063.

[44] Y. Deng, C. Wan, C. Li, Y. Wang, X. Mu, W. Liu, Y. Huang, P.K. Wong, L. Ye, Synergy Effect between Facet and Zero-Valent Copper for Selectivity Photocatalytic Methane Formation from CO$_2$, ACS Catal. 12 (2022) 4526–4533.

[45] J. Sheng, Y. He, J. Li, C. Yuan, H. Huang, S. Wang, Y. Sun, Z. Wang, F. Dong, Identification of Halogen-Associated Active Sites on Bismuth-Based Perovskite Quantum Dots for Efficient and Selective CO$_2$-to-CO Photoreduction, ACS Nano 14 (2020) 13103–13114.

[46] X. Li, L. Li, G. Chen, X. Chu, X. Liu, C. Naisa, D. Pohl, M. Loffler, X. Feng, Accessing parity-forbidden d-d transitions for photocatalytic CO$_2$ reduction driven by infrared light, Nat. Commun. 14 (2023) 4034.

[47] I.V. Chernyshova, S. Ponnurangam, P. Somasundaran, Linking interfacial chemistry of CO$_2$ to surface structures of hydrated metal oxide nanoparticles: hematite, Phys. Chem. Chem. Phys. 15 (2013) 6953–6964.

[48] J. Wu, X. Li, W. Shi, P. Ling, Y. Sun, X. Jiao, S. Gao, L. Liang, J. Xu, W. Yan, C. Wang, Y. Xie, Efficient Visible-Light-Driven CO$_2$ Reduction Mediated by Defect-Engineered BiOBr Atomic Layers, Angew. Chem., Int. Ed. 57 (2018) 8719–8723.

[49] X. Bao, M. Zhang, Z. Wang, D. Dai, P. Wang, H. Cheng, Y. Liu, Z. Zheng, Y. Dai, B. Huang, Molten-salt assisted synthesis of Cu clusters modified TiO$_2$ with oxygen vacancies for efficient photocatalytic reduction of CO$_2$ to CO, Chem. Eng. J. 445 (2022) 136718.

[50] N. Li, X.-P. Zhai, B. Ma, H.-J. Zhang, M.-J. Xiao, Q. Wang, H.-L. Zhang, Highly selective photocatalytic CO$_2$ reduction via a lead-free perovskite/MOF catalyst, J. Mater. Chem. A 11 (2023) 4020–4029.

[51] R. Zhang, H. Wang, S. Tang, C. Liu, F. Dong, H. Yue, B. Liang, Photocatalytic Oxidative Dehydrogenation of Ethane Using CO$_2$ as a Soft Oxidant over Pd/TiO$_2$ Catalysts to C$_2$H$_4$ and Syngas, ACS Catal. 8 (2018) 9280–9286.

[52] I.A. Fisher, A.T. Bell, In Situ Infrared Study of Methanol Synthesis from H$_2$/CO over Cu/SiO$_2$ and Cu/ZrO$_2$/SiO$_2$, J. Catal 178 (1998) 153–173.

[53] Z. Zhang, D. Li, Z. Dong, Y. Jiang, X. Li, Y. Chu, J. Xu, Lead-Free Cs$_2$AgBiBr$_6$ Nanocrystals Confined in MCM-48 Mesoporous Molecular Sieve for Efficient Photocatalytic CO$_2$ Reduction, Sol. RRL 7 (2023) 2300038.

[54] F. Xu, K. Meng, B. Cheng, S. Wang, J. Xu, J. Yu, Unique S-scheme heterojunctions in self-assembled TiO$_2$/CsPbBr$_3$ hybrids for CO$_2$ photoreduction, Nat. Commun. 11 (2020) 4613.

[55] L. Wang, B. Cheng, L. Zhang, J. Yu, In situ Irradiated XPS Investigation on S-Scheme TiO$_2$@ZnIn$_2$S$_4$ Photocatalyst for Efficient Photocatalytic CO$_2$ Reduction, Small 17 (2021) 2103447.